An Energy Spectrum Algorithm for Wind Direction Retrieval From *X*-Band Marine Radar Image Sequences

Hui Wang, Haiyang Qiu, Zhizhong Lu, Lei Wang, Rizwan Akhtar, and Yanbo Wei

***Abstract*—In this study, an energy spectrum (ES) algorithm is proposed to retrieve wind direction from *X*-band marine radar image sequences. This algorithm is based on utilizing the occlusion area zero-pixel percentage to distinguish rain-free and rain-contaminated radar data. And then the rain-contaminated images are detected and discarded. The effect of radar radial attenuation in radar image sequences is modified by the piecewise fitting technique. Wind direction is determined from rain-free and radial correction data, based on the ES of small-scale wind streaks. The ES of small-scale wind streaks is obtained by establishing an ES scale separation filter. Based on the wind streak characteristics, a 2-D fast Fourier transform is used to obtain the ES of radar images. The wind streak characteristics are derived from the distribution of the azimuth normalization radar cross section. The proposed algorithm is tested using data collected from *X*-band radar images and *in situ* anemometer data from the coast of the East China Sea. Compared with the anemometer data, after using the proposed algorithm, the root-mean-square difference for wind direction is 12.13°, which is an acceptable result for engineering application.**

***Index Terms*—Energy spectrum (ES), radial correction, rain recognition, wind direction, *X*-band marine radar.**

I. Introduction

SEA SURFACE wind is an important factor in ocean dynamics, and significant to marine exploration, navigation safety, and on- and off-ships activities [1]. The sea surface wind field based on marine radar inversion is one of the important environmental factors for continuous and real-time takeoff and landing safety of carrier-borne aircraft under the condition of sea dynamic vehicle. When carrier-borne aircraft takeoff and land, they usually pay attention to the steady wind speed and direction parameters on the ship surface. It is defined as the average value in space and time of free flow undisturbed by barrier structures, and be directly used to adjust the upwind angle of carrier-borne aircraft when taking off and landing with high requirement of measurement accuracy. Current technology usually calculates this information through *in situ* sensors located on the ship's mast. However, the application of this conventional method is based on the assumption that the flow field in the area conforms to the free flow. In practice, this assumption is difficult to realize due to the limited sensor layout and ship surface structure. Therefore, the measurement of wind field parameters error is too large to meet the needs of users. The average wind field information retrieved from marine radar is the sea surface near 1 km from the ship. The unique measurement area is free of structural disturbance and tends to be closer to free flow. It provides more accurate steady-state wind parameters on the ship surface for carrier aircraft. *In situ* wind measurement by anemometers refers to a cup or ultrasonic wind meter mounted on the ship's mast or buoy [2]. The sensors placed on mast are affected by the ship surface structure and those on the buoys cannot move with the ships, so the real-time sea surface wind field information of navigation is difficult to acquire continuously. When extracting the wind field information in the vicinity of the ships, the ships need to stop sailing and drop the buoy for measurement. After the measurement, the buoys need to be recovered, which is inconvenient and expensive to use. In recent decades, *in situ* remote-sensing instruments such as synthetic aperture radar (SAR) [3], [4], high-frequency (HF) radar [5], [6], and *X*-band marine radar have been broadly used to retrieve sea surface wind [7]. *X*-band marine radar has high spatial and temporal resolution, as well as a low extra cost relative to other remote-sensing instruments [8]. This type of radar has frequently been mounted on ships and other vessels for navigation purposes [9], providing a convenient means for studying sea surface inversion data, such as oil spill detection[10], surface current [11]–[13], wave height [14]–[16], and other factors.

Wind direction retrieval using *X*-band marine radar image sequences is a much more attractive approach than using an

Manuscript received December 14, 2020; revised February 13, 2021 and March 8, 2021; accepted March 22, 2021. Date of publication March 31, 2021; date of current version April 22, 2021. The work was supported in part by the National Natural Science Foundation of China under Grant 41906154, in part by the Natural Science Foundation of Jiangsu Province, China under Grant BK20180988, and in part by the Natural Science Foundation of Higher Education Institutions of Jiangsu Province under Grant 19KJB510024. *(Corresponding author: Zhizhong Lu.)*

Hui Wang is with the Jiangsu University of Science and Technology, Jiangsu 212003, China, and also with the Department of Electronic Information, Jiangsu University of Science and Technology, Zhenjiang 212003, China (e-mail: wanghuijkd@just.edu.cn).

Haiyang Qiu is with the Jiangsu University of Science and Technology, Jiangsu 212003, China (e-mail: hy.qiu@just.edu.cn).

Zhizhong Lu is with the Harbin Engineering University, Harbin 150001, China, and also with the Department of Automation, Harbin Engineering University, Harbin 15001, China (e-mail: luzhizhong@hrbeu.edu.cn).

Lei Wang is with the State Key Laboratory of Information, Wuhan University, Wuhan 430079, China (e-mail: lei.wang@whu.edu.cn).

Rizwan Akhtar is with the Electronics and Information School, Jiangsu University of Science and Technology, Zhenjiang 212013, China (e-mail: rizwanakhtarpk@gmail.com).

Yanbo Wei is with the College of Physical and Electronic Information, Luoyang Normal University, Luoyang 471022, China (e-mail: weiyanbo@hrbeu.edu.cn).

Digital Object Identifier 10.1109/JSTARS.2021.3069989

anemometer. Given its high resolution and real-time feedback, it can be utilized in most weather conditions [17]. Huang [18] presented a comprehensive review of current marine information retrieval techniques, which validated the feasibility of using *X*-band marine radar to measure ocean winds and waves. At present, there are two means used to retrieve wind direction from *X*-band marine radar image sequences. The first utilizes the relationship between the normalized radar cross section (NRCS) and radar look direction [19], the wind direction retrieved from this relationship requires the entire 360°azimuth echo, which is difficult to acquire for radars deployed at the coast due to sheltering by the land. An improved method, which does not require the entire azimuth, was analyzed in [20], but the consecutive radar images must guarantee that the azimuth cover is larger than 180°. Liu *et al.* [21] proposed an ensemble empirical mode decomposition method to retrieve wind direction from radar, which yielded good results for retrieving the sea surface wind direction from low wind speed rainfall images, although full 360° unobstructed radar images are still required. The second retrieval method is based on the visible streaks induced by wind in radar images [22]. There are quite a few algorithms utilizing this factor, among which the optical flow-based motion estimation technique (OFM) [23] and the local gradient method (LGM) [24] are commonly used. Nevertheless, the result of the OFM algorithm is less accurate and cannot satisfy real-world project requirements. The LGM must further iteratively smooth and subsample the wind streak images in order to obtain the so-called Gaussian pyramid. Experiments have clearly revealed that accurate wind direction results can only be obtained when the image resolution is reduced to 1/16–1/4 of the wind streak scale. Wind streaks, however, have an indeterminate spacing of 200–500 m, thus making it difficult to automatically determine the appropriate image resolution for retrieval. Moreover, if a fixed image resolution is used, there will be inconsistent wind direction error. A method based on radar image texture was first generated based on spatial variability analysis in [25]. This approach improves the wind direction retrieval ability from rainfall images, although the filtering process will filter out useful wind-related information in the original image, which reduces the accuracy of wind direction inversion.

The retrieval of sea surface information using *X*-band marine radar will be influenced by rainy conditions [26]. In general, the rain has the following four significant effects on the NRCS of the marine radar:

1) radar receives the raindrops induce volumetric scattering signal;
2) radar microwave signal attenuate by rainfall;
3) raindrops striking the water surface will alter roughness of the ocean surfaced;
4) airflow associated with a rain event may change the original wind field of sea surface [27], [28].

Although previous filtering algorithms play an important role in target detection [29], these techniques do not work well in sea surface retrieval using rain-contaminated radar images. Therefore, a rainfall-recognition algorithm, which can guarantee an accurate retrieval rate, is necessary in the case of rainfall. Chen and Huang [30] proposed an unsupervised learning approach to identify rain-contaminated and low-back scatter regions in *X*-band marine radar images using texture features and SOM-based clustering techniques. Then they proposed a type of deep neural network to detect and locate rain-contaminated pixels in *X*-band marine radar images. The detector can segment rain-contaminated regions by classifying each pixel into three classes—rain-free, rain-contaminated, and wind-dominated rain cases [31]. These methods solve the problem of identifying the rain-contaminated regions in the image, but the wind retrieval algorithm proposed in this article is in the rain-free image, so the rainfall image threshold filtering method is chosen in this article to eliminate rain-contaminated images. In [17], it was also found that the zero-pixel percentage (ZPP) rainfall recognition algorithm depends on the zero-intensity percentage of the entire radar image. The NRCS of the entire image is easily affected by sea waves, currents, the wind field, and other factors, however, usually resulting in a high NRCS. Hence, the obtained ZPP recognition threshold will be too low to effectively identify the rainfall image. The method of rainfall image recognition based on support vector machines is proposed in [32]. Compared with ZPP, the accuracy of rainfall recognition is improved, although each image requires n-dimensional vector transformation, which cannot solve the problem of real-time monitoring. 1-D complex continuous wavelet transform was proposed in [33] to correct the influence of rain on gray-level radar images, but this method is time consuming and unsuitable for multimodal seas.

In this study, we propose a new algorithm for retrieving wind direction based on the energy spectrum (ES) of wind streaks in rain-free radar images, an approach that utilizes the occlusion radar image ZPP to improve the effectiveness of rainfall identification. Radial correction of the image must be carried out before using the algorithm. Otherwise, the radial attenuation of the image will lead to the formation of an inherent symmetric spectrum of the ES, which will interfere with the subsequent wind direction results. The piecewise fitting method is used to correct the attenuation of radar images. The rest of this article is organized as follows. An overview of the instrumentation and data are presented in Section II. The wind field imaging characteristics and small-scale wind streak characteristics are described in Section III. In Section IV, the wind direction retrieval method is introduced. The results of the wind direction retrieval are validated, and the range and sensitivity of errors are discussed in Section V. Finally, a summary is presented in Section VI.

II. Data Overview

The radar utilized in this study is a standard RM-1290 *X*-band marine radar, operating at grazing incidence with horizontal polarization in transmission and receiving (HH). The RM-1290 is a short-pulsed radar, with a pulsewidth of 0.5–10 μs. The radar operates at 9.4 GHz, with a sampling frequency of 20 MHz. Fig. 1 shows the research platform with its 55 m-long mast. The 1.8-m open array antenna is mounted on the main mast at a height of 40 m above sea level with a 1.3° horizontal beamwidth. The radar antenna rotates with a period of 2.5 s (24 r/min) and has a pulse repetition frequency of 1.3 kHz. The radar spatial

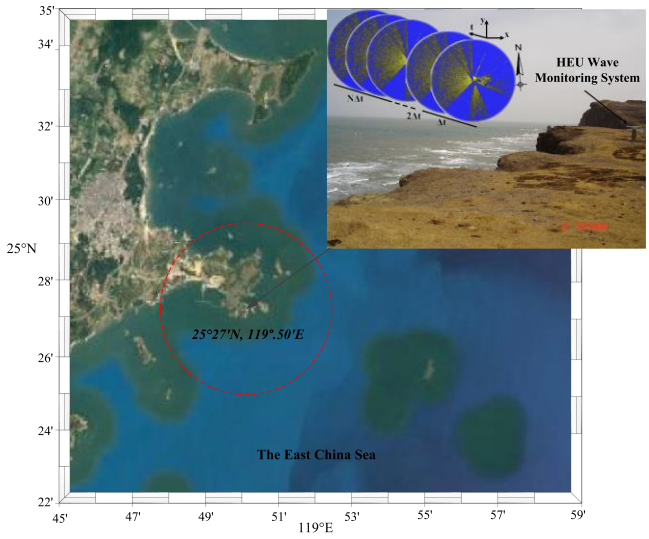

Fig. 1. Research platform and radar image sequences of the HEU wave monitoring system at the East China Sea.

resolution is 7.5 m in range and 0.1° in azimuth, covering an area with a radius of ∼4300 m. The study area covered the range from 600 to 2100 m.

The WaMoS, Wavex, and HEU wave and current monitoring systems are connected to the radar platform, which is located on the shore of Haitan Island along the East China Sea, the position was 25° 27′ N, 119° 50′ E. The radar image sequence collected from the HEU wave monitoring system consisted of 32 images lasting 80 s. The data used for the present work were collected within the last system, which digitized and stored the spatial and temporal radar backscatter information as a sequence of images with a 14-bit grayscale depth, i.e., digitized backscatter intensities ranging from 0 to 8192. Each of the radar image sequences collected here consisted of 32 images representing an 80-s period. The radar image sequence depicted a wave field propagating in an easterly direction. The northern quadrant of the image was masked (white sector) starting from the shore. This white sector area was excluded from investigation with the HEU wave monitoring system, which is capable of measuring the spatial and temporal evolution of the surface wave field.

The reference data used to validate the radar-based wind retrieval scheme developed here were acquired from a vane anemometer. The vane anemometer used for measuring the single-point wind data was part of an R. M. Young Model-05103 wind field monitor. The wind field monitor was located on the top of the main mast at a height of 55 m above sea level, and could record the wind direction and wind speed data once per minute.

The data used in this study were collected before and after Typhoon Megi ("Catfish") during October 2010–November 2010, totaling 1634 acquisition times with wind speeds up to 20 m/s. The main mast was located in a water depth of 28 m, as shown in Fig. 1. It should be noted that not all data were utilized in this study due to rainfall and the typhoon. For comparison with the actual wind speed, the reference wind speed needs to be converted to the value at 10 m of the sea surface. We used

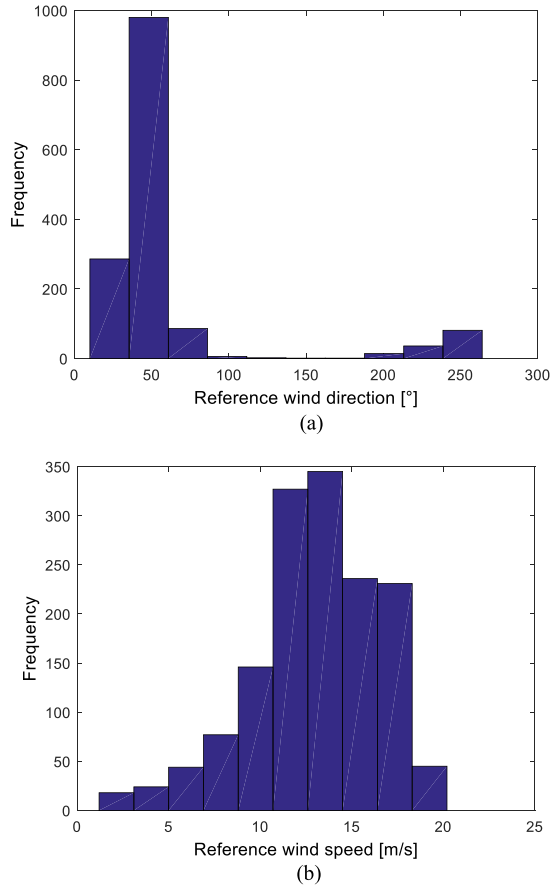

Fig. 2. Distribution of reference wind direction and wind speed. (a) Distribution of reference wind direction. (b) Distribution of reference wind speed.

a factor of approximately 1.2, i.e., $U_{10} = U_{55}/1.2$. This factor was estimated using ln(55/z0)/ln(10/z0), assuming z0 to range from 1 mm to 1 cm [34]. The data distributions of the reference wind direction and wind speed are presented in Fig. 2. This figure shows that the wind direction covered 10°–264°, since part of the sea surface wind direction could not be collected due to the shore-based observation. The wind direction with the highest frequency was approximately 50°, while the wind direction of ∼200° was caused by the transitional wind reversal from Typhoon Megi passed. The reference wind speed was distributed in the range of 1.2–20.1 m/s, with a greater frequency occurring within the 8–15 m/s range, and lower frequencies in the high and low wind speed ranges.

III. Research and Extraction of Scale Wind Streak Characteristics

In airborne or spaceborne SAR images, there are both large-scale wind streaks of 1–8 km and small-scale wind streaks of 100–500 m [35], [36]. Research has revealed that the large-scale wind streaks are caused by the flow of air in the free atmosphere under the action of buoyancy [37], while the small-scale streaks are generated by wind shear stress. According to the imaging mechanism of *X*-band marine radar, the sea surface wind field appears in the form of small-scale wind streaks in *X*-band marine radar images.

Some streaks form, evolve, and decay over relatively short lifetimes of dozens of minutes, and then rapidly regenerate, hence the label "small-scale wind streak" [38]. It has been found that the light and dark stripes modulated by wind fields exist in navigation radar images. Experimental results have revealed that the changes in roughness caused by the turbulence of wind shear stress can be detected by marine radar, and these results can be reflected in radar images as a striped distribution. The relationship between the near-surface wind vector and the NRCS can be described by a geophysical model function (GMF) [23].

To obtain a more pure small-scale wind streak image, we performed timing integration on a set of radar image sequences (consisting of 32 images) collected from the monitoring system. The static patterns of the sea surface features with low-frequency signals (including sea surface wind field information) were obtained after filtering out HF wave noise. This approach is analogous to establishing a low-pass filter, with only frequencies lower than the integration time remaining, such as static and quasi-static signals, while other signals were removed. This process can be expressed by the following formula:

$$f(r,\theta) = \frac{\sum_{t=0}^{N_t} f'(r,\theta,t)}{N_t} \tag{1}$$

where $f(r,\theta)$ is the static feature image of the sea surface, $f'(r,\theta,t)$ represents a single image in the radar image sequence, and N_t is the number of images, which in this study was 32. Fig. 3(a) shows a wave pattern radar image. To accurately reflect the modulation characteristics of wind waves, an area with a radial radius of 600–2100 m in the radar image was utilized, and a range of 106°–291° amplitude in the radar image was selected to remove the influence of shore-based stationary target noise. Fig. 3(b) shows a static feature image of the sea surface, in which the small-scale wind streaks are within the black square.

Fig. 4(a) presents the NRCS in an azimuthal mapping distribution diagram. This figure was derived from the radial normalization of the region within the black square in Fig. 4(b). By comparing the wave streaks and wind streaks in Fig. 4(a), we find that the wave streaks changed more dramatically than the wind streaks, with the scale distribution exhibiting large differences in the figure. The results of the azimuthal mapping calculation for the wind streaks revealed that there were approximately 40-pixel points, and the pixel resolution was about 7.5 m; hence, the mapping scale was 300 m. Meanwhile, the wave streak mapping pixel point number was about 16, with a mapping scale of 120 m.

By performing statistical analysis on 40 sets of radar image sequences, in which the wind directions range from 31° to 45° and the wind speeds range from 15.3 to 19.1 m/s, the scale range of the sea surface static features was obtained. As shown in Fig. 4(b), the lower limit of the small-scale wind streaks was 200 m and the upper limit was 500 m. Hence, the scale was determined to range from 200 to 500 m, and the wind streak is aligned with the wind direction.

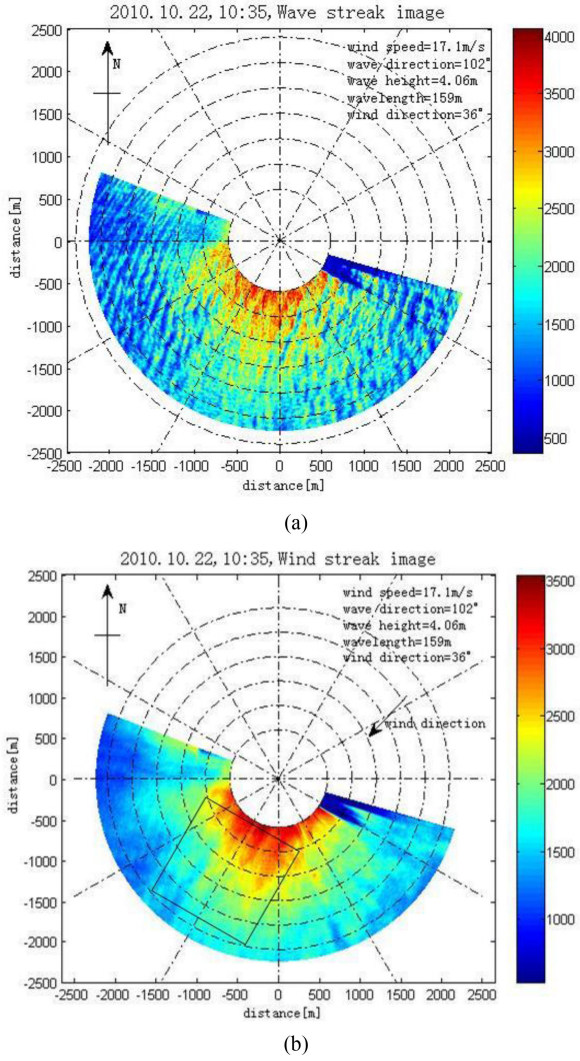

Fig. 3. (a) Wave patters radar image collected on October 22, 2010. (b) Static feature image of sea surface got from the radar image sequences on October 22, 2010. The wind speed during measurement was 17.1m/s, the wind direction was 36°. The direction spread of the wave-propagation direction was 102°.

IV. Wind Direction Retrieval

In this section, we introduce a proposed ES method to retrieve wind direction from *X*-band marine radar data. In the spatial domain, retrieval performance is difficult to guarantee when small-scale wind streak characteristics are not apparent. On the basis of the FFT method, sea surface wind direction can be extracted from SAR images. Therefore, we propose a type of modified FFT method to retrieve wind direction from radar-image sequences to improve the retrieval accuracy and data applicability.

That MABL rolls modulate the sea surface roughness leads the large-scale wind streaks on the SAR image. It is because that roughness is sensed by SAR via the change of the Bragg wave spectrum. The mechanisms for generating atmospheric boundary layer rolls can be attributed to dynamic or thermodynamic instability in the boundary layer [39], [40]. These large-scale wind streaks range from 1 to 8 km, and their axis is nearly consistent with the wind direction on the sea surface. Based on these findings, Koch [41] was the first to determine a 2-D wave-number spectrum of a SAR subimage.

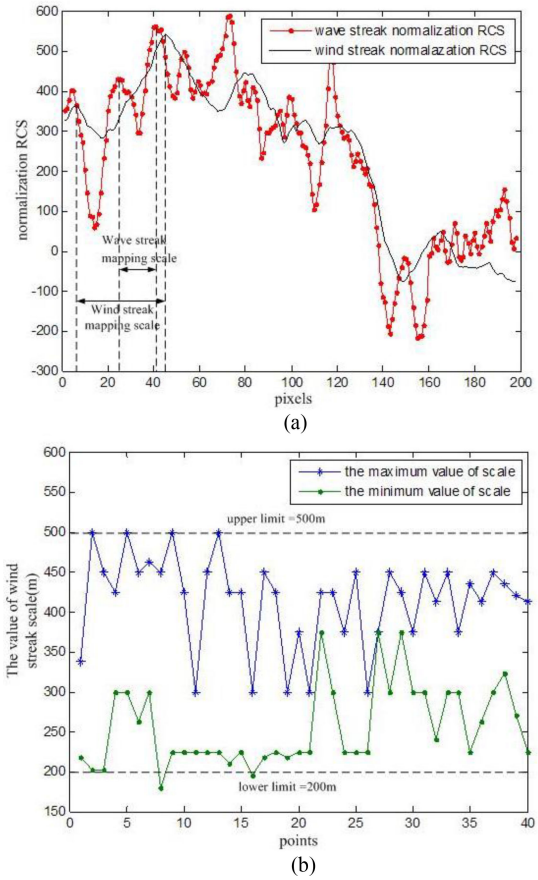

Fig. 4. (a) NRCS in azimuth mapping distribution diagram. (b) Maximum and the minimum streak scales of static feature images extracted from 40 groups of image sequences.

Connecting the centers of two symmetrical peaks in the ES, the direction of the connecting line indicates dramatic changes in the radar image, i.e., the gradient direction of large-scale wind fringes. The vertical axis from the connecting line is the direction of the large-scale wind streak, which can be identified as the sea surface wind direction of the subimage. Hence, the sea surface wind directions of all subimages can be obtained.

Since large-scale streaks depicted by SAR are directly displayed on the radar image, the sea surface wind direction information can be extracted directly from the ES of the SAR image. For marine radar, however, owing to the modulation effect from the sea surface wind field, the small-scale wind streaks in the radar images are completely different from those in the SAR images in terms of period and scale characteristics, and these wind streaks cannot be directly displayed in a single marine radar image. Usually, the small-scale wind streaks are easily overshadowed by the rainfall signal, a phenomenon that is similar to radar image attenuation. Therefore, these small-scale wind streaks in marine radar images are hard to extract. In this section, inspired by the extraction method used for SAR, we propose an ES method to extract the sea surface wind direction from marine radar images. First, the occlusion area ZPP (OZPP) rain recognize method is used to identify rainfall image sequences. Then adaptive segment fitting correction method is used to correct the radial direction of the radar image. After correcting, apply temporal integration to obtain the static feature containing wind streaks. Finally, the wind direction is retrieved from the proposed ESM.

A. Rain Recognition

Since the ES method only works for rain-free radar images, the images must be automatically selected based on rain recognition data preprocessing. When studying the inversion of sea surface wind field from the measured data of *X*-band navigation radar, Lund *et al.* [8] found that the overall echo intensity value significantly increased, while the proportion of zero-intensity pixel points significantly decreased in radar images because of the rainfall. Based on these findings, he proposed to use the proportion of zero-intensity pixel points in the entire radar image to identify rainfall radar images. Considering the influence of sea conditions on the statistical results, this study extended this method to rainfall recognition based on the zero-intensity percentage in the occlusion area of radar images.

Because the radar works in a particular environment, a certain proportion of invalid signals are generated in collected radar images. In the case of rainfall, radar echoes are apparent in shaded areas where the radar beam is blocked by the surface crest, indicating that raindrop scattering plays an important role in the atmosphere. Therefore, under the same sea conditions, the presence of rainfall will reduce the proportion of low-back signals in a radar image. Based on practical experience with sea surface echo region processing, radar echo signals with echo voltage values smaller than 0.3 V are usually regarded as invalid. In this study, the echo intensity value of the pixel points corresponding to invalid signals was set as zero, and the proportion of pixel points with zero intensity in the radar image was defined as the percentage of zero intensity. Based on the original *X*-band marine radar image file storage format, the radar echo signal strength of any pixel could be converted into a voltage value ranging from 0 to 2.5 V. All points with voltage values smaller than 983 were then eliminated after normalization of the intensity (according to the storage protocol, 0.3 V was equivalent to an intensity value of 983), and the proportion of the intensity of the zero pixels was then calculated. The zero strength percentage formula from [8] is

$$P = \frac{f_0}{f} \tag{2}$$

where f is the sum of pixels in a radar image, and $f_0$is the number of normalized zero-intensity pixels.

For marine radar images, when the propagation path of the radar electromagnetic wave is blocked due to obstacles such as chimneys, masts, islands, and so on, a large number of invalid signals will be generated in the radar image, resulting in a fan-shaped shadow area (occlusion area) in the image. When there is no rain, the occlusion area is depicted as almost completely blue, indicating no radar echo. When there is rainfall, the raindrops can reflect the radar electromagnetic wave signal and generate uniform backscattering, causing the blocked area to exhibit flaky rain echoes. Since the zero-intensity percentage

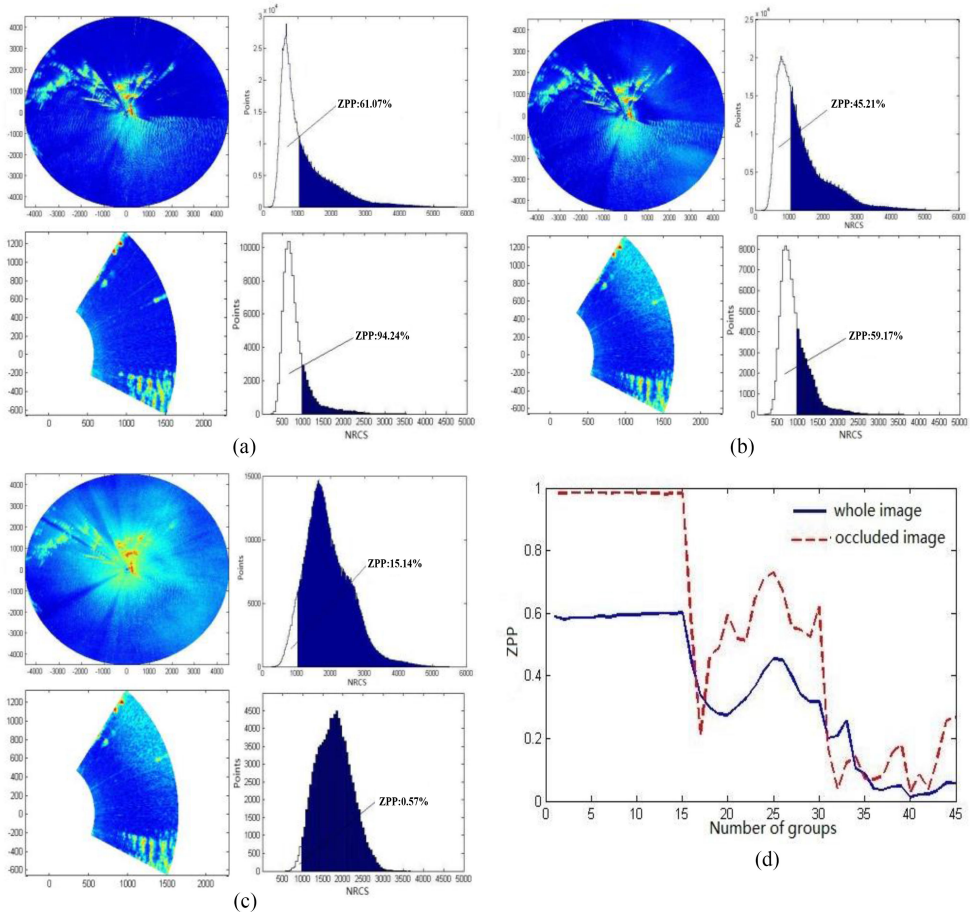

Fig. 5. Echo intensity histogram plots of both the entire image and the partially cropped occlusion area for (a) rain-free, (b) light rain, and (c) heavy rain conditions. The zero-intensity pixel percentage is plotted in panel (d).

of the statistical occlusion area will not be affected by the change of sea conditions, it is more effective and accurate for detecting whether the radar image is affected by rainfall. In this study, we selected 45 groups of radar images of no rain, light rain, and heavy rain conditions, plotted the echo intensity histograms of the entire images and the partially cropped occlusion areas, and calculated the zero-intensity pixel percentages, as shown in Fig. 5.

According to Fig. 5(a), when there was no rain, the entire and occlusion radar image ZPPs were 61.07% and 94.24%, respectively. When there was light rain, the entire and occlusion radar image ZPPs were significantly lower, with corresponding values of 45.21% and 59.17%, as shown in Fig. 5(b). When the rainfall intensity is relatively high, the rainwater basically covers the occlusion area, with the zero-intensity percentage of the entire occlusion area falling to 0.57% and the ZPP of the entire radar image decreasing to 15.14%, as shown in Fig. 5(c). This demonstrates that the statistical result of the zero-intensity percentage of the cropped occlusion area image is much larger than that of the entire radar image, and the zero-intensity percentage of the occlusion area will be more effective and accurate for determining whether the radar image is influenced by rainfall.

Fig. 5(d) shows the ZPP distribution of the two types of radar images for the three different weather conditions. In the case of no rainfall, the ZPP values of both images are relatively large, but the OZPP is higher. As the rainfall intensity increases, the zero-intensity percentage decreased, although the changing trend of the OZPP is much more obvious, especially in the occlusion images. Therefore, based on the OZPP difference between radar images in rainfall and nonrainfall conditions, the corresponding threshold value could be selected to identify the rainfall and nonrainfall radar images.

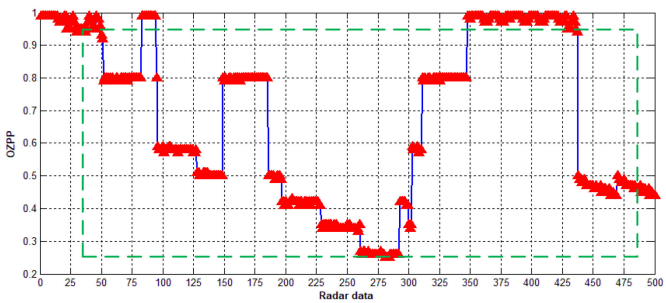

Fig. 6. OZPP distribution of 500 radar images. (The green dotted rectangular area in the figure is the data of rainfall in the radar image).

Fig. 6 shows the OZPP distribution of 500 radar images, in which the selected radar region consists of 80–600 pixels in the

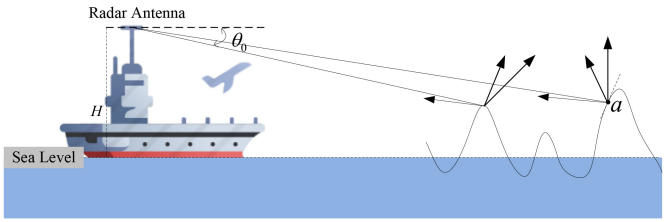

Fig. 7. Working mechanism of marine radar; θ_0 is the grazing incidence angle, a is the Bragg scattering point.

radial direction and 50–90 pixels in the azimuthal direction. The dashed rectangular area in Fig 6 encompasses the rainfall data in the radar image. When there is no rain, the OZPP maintains a stable change range, very close to 1, because there are almost no radar echoes. When rainfall occurred, the zero-intensity percentage in the occlusion area decreases immediately by a significant amount. Finally, based on the statistical results, 0.94 is selected as the threshold for detecting whether the radar image was affected by rainfall. Hence, when the OZPP is larger than 0.94, it indicates that there is no rainfall in the detection area; when OZPP is smaller than 0.94, it can be deduced that there is rainfall in the detection area.

B. Image Correction

As shown in Fig. 3(b), the small-scale wind streaks attenuate when the radial distance increases (as indicated by the color becoming blue). This attenuation is caused by the working mechanism of the marine radar, as illustrated by the geometrical diagram presented in Fig. 7. For *X*-band radar, when the NRCS is proportional to the spectral density of the surface roughness, the main backscatter mechanism at the ocean surface is Bragg scattering [20]. Marine radar receives microwaves to form a sea clutter image, but the NRCS in the image will reduce as the radial distance increases. This will corrupt wind streaks and the inherent attenuation differentiation spectrum, ultimately lead to the deterioration of retrieval precision.

Radial attenuation has little effect on the retrieval of HF signals such as surface current and significant wave heigh. However, it has great influence on the inversion of sea surface wind direction by wind streaks. As shown in Fig. 3(b), wind streaks become gradually blurred as their distance from the center position increases, and are barely visible when the radial distance is over1500 m. Thus, radial attenuation cannot be ignored when we retrieve wind information from marine radar images.

Fig. 8 shows the range-averaged NRCS of Fig. 3(a). The subplots show the radial NRCSs with different amplitudes. Fig. 8(f) shows that radial NRCS mean value of the entire selected sector also decays in an irregular manner. However, the radial attenuation exhibits a trend with increasing radial distance, although there is no fixed model to account for the relationship between the radial attenuation and increasing radial distance, and the models are usually nonlinear.

Fig. 9 shows the ES of the static feature image of a sea surface [the area within the black square in Fig. 3(b)], in which there are two pairs of high-energy symmetric areas relative to the origin. According to the wind streak characteristics, the bilaterally symmetric energy areas are wind streak energy spectra, while the vertically symmetric energy areas are radial attenuation energy spectra because that the radial attenuation is perpendicular to wind streak. According to the radar imaging definition, the relationship between wavelength L and wavenumber k is $L = \frac{2\pi}{k}$. Therefore, these radial attenuation streaks have a typical spacing of 200–500 m and belong to the static state, nonlinear signal. Since the radial attenuation characteristics are similar to those of the wind streaks, the radial attenuation signal cannot be separated from the wind streaks in the static feature image. To address this problem, we developed a relative radiometric correction method to reduce the effect of radial attenuation.

This method, as described below, consists of two parts. First, in steps 1–5, an adaptive Lagrange least-square piecewise fitting approach is proposed for acquiring the fitting NRCS, and the fitting NRCS is then used in step 6 to correct the images.

Step 1: Average the single radar image along the azimuthal direction, and define the NRCS of a single image as $\sigma(\theta_i, \mathrm{r}_j)$ $(i = 1, 2, \cdots P, j = 1, 2, \cdots Q)$, where P and $Q$are the azimuth and radial direction pixel numbers, so that the 1-D radial NRCS y can be written as

$$y = \frac{1}{P}\sum_{i=1}^{P}\sigma(\theta_i, \mathrm{r}_j) \tag{3}$$

If radial r_j is defined as x , then x and y generate a dataset $\Omega = \{(x_i, y_i)\}_{i=1}^{n}$, where n is the total number of data points.

Step 2: Suppose the discontinuity number of datasets $\Omega$is K. There will then be $K+1$subdatasets $\Omega_k = \{(x_i^k, y_i^k)\}_{i=1}^{n_k}$, $k = 1, 2, \cdots K+1$, in which the points of the kth subdataset is represented by n_k, and $x_{k-1} \le x_i^k \le x_k$, where $x_k$is the segment point of Ω_k and Ω_{k+1}.

Step 3: Define the fitting function of dataset Ω as $f(x)$, with $f(x)$ taking the form

$$f(x) = \begin{cases} f_1(x) = \sum_{j=1}^{m}\alpha_j^1 h_j(x), 1 \le x \le x_1 \\ f_2(x) = \sum_{j=1}^{m}\alpha_j^2 h_j(x), x_1 \le x \le x_2 \\ \vdots \\ f_k(x) = \sum_{j=1}^{m}\alpha_j^2 h_j(x), x_{k-1} \le x \le x_k \\ \vdots \end{cases} \tag{4}$$

where$f_{k-1}(x_k) = f_k(x_k)$, $\{h_j\}_{j=1}^{m}$ is the basic function of subdataset Ω_k, which generally takes a simple function form. For computational convenience, we selected $1, x, x^2$ as the basic function. The number of basic functions is m , and we chose $m = 3$.$\{\alpha_j^k\}_{j=1}^{m}$ are the regression coefficients that need to be determined. To ensure that the fitting error is minimized and the fitting function is continuous at the pointx_k, the least-squares

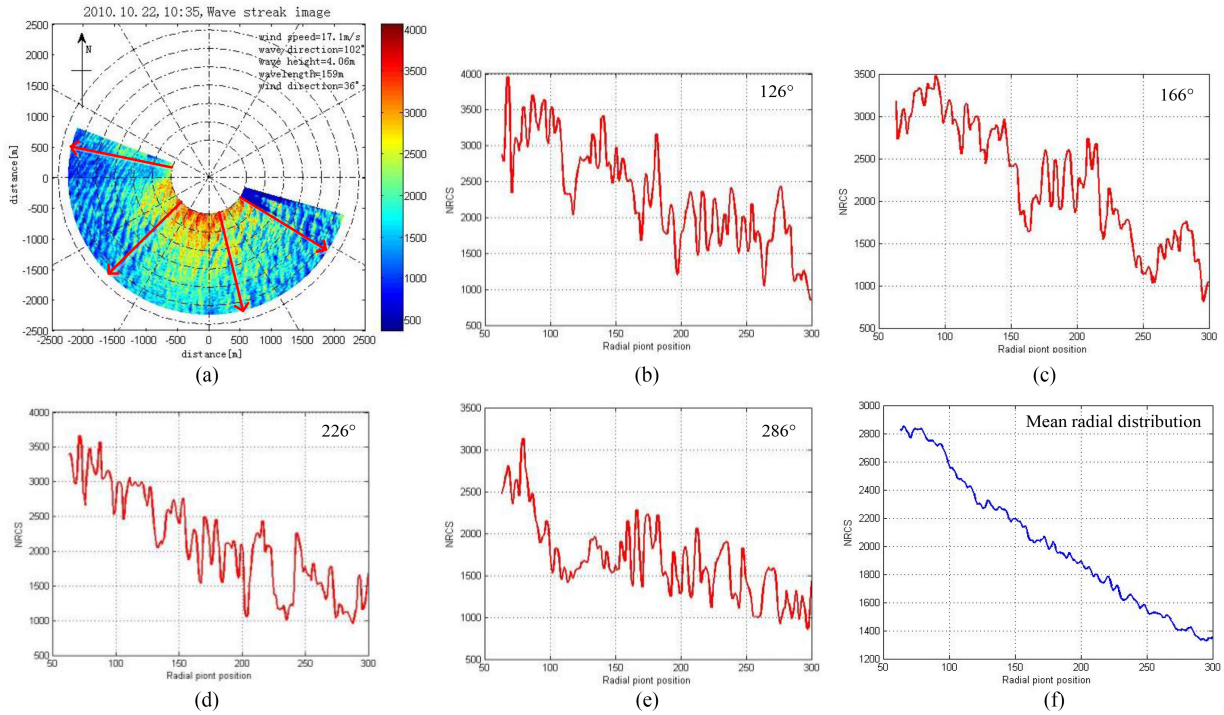

Fig. 8. Mean NRCS of Fig. 3(a). The red arrows show directions selected along the radial amplitude angle. Subplots b, c, d, and e are the radial distributions corresponding to the selected directions 126°, 166°, 226°, and 286°; f shows mean radial distribution.

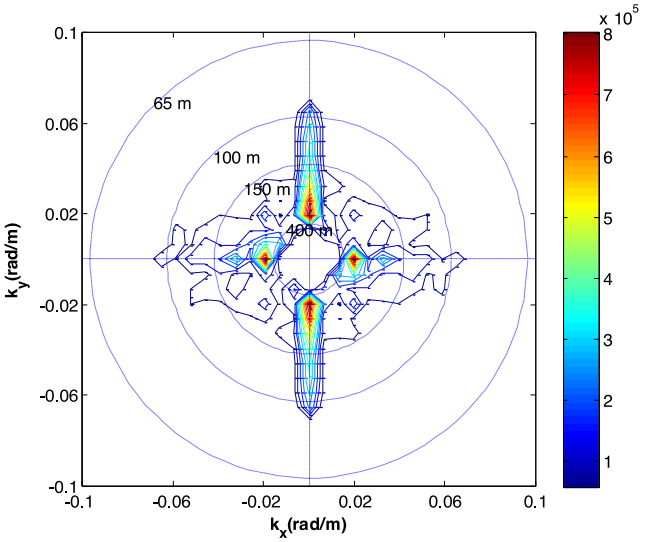

Fig. 9. Energy spectra of the sea surface static feature image [the area within the black square in Fig. 3(b)]; k_x and k_y are the components of wavenumber k.

regression model is constructed as follows:

$$\min_{\alpha_j^k} \sum_{i=1}^{n_1} \left(f_1(x_i^1) - \mathrm{y}_i^1\right)^2 + \sum_{i=1}^{n_2} \left(f_2(x_i^2) - \mathrm{y}_i^2\right)^2 + \cdots + \sum_{i=1}^{n_k} \left(f_k(x_i^k) - \mathrm{y}_i^k\right)^2 + \cdots \sum_{i=1}^{n_k} \left(f_{K+1}(x_i^{K+1}) - \mathrm{y}_i^{K+1}\right)^2$$
$$s.t. f_{k-1}(x_k) = f_k(x_k). \tag{5}$$

The basic function is $h(x) = [1 \quad x \quad x^2]$, and the row vector fitting parameters are

$$X_k = \begin{bmatrix} h(x_1^k) \\ h(x_2^k) \\ \vdots \\ h(x_{n_k}^k) \end{bmatrix}, \quad y_k = \begin{bmatrix} y_1^k \\ y_2^k \\ \vdots \\ y_{n_k}^k \end{bmatrix},$$
$$\alpha_k = \begin{bmatrix} \alpha_1^k \\ \alpha_2^k \\ \alpha_3^k \end{bmatrix}, \quad (k = 1, 2, \cdots K+1).$$

The multiple-segment dataset fitting parameters can be expressed as

$$Y = \begin{bmatrix} y_1^T \\ y_2^T \\ \vdots \\ y_{K+1}^T \end{bmatrix} \alpha = \begin{bmatrix} \alpha_1^T \\ \alpha_2^T \\ \vdots \\ \alpha_{K+1}^T \end{bmatrix} X = \begin{bmatrix} X_1 & 0 & \cdots & 0 \\ 0 & X_2 & \cdots & 0 \\ \vdots & \vdots & & \vdots \\ 0 & 0 & \cdots & X_{K+1} \end{bmatrix} Z$$
$$= \begin{bmatrix} h(\mathrm{x}_1) & -h(\mathrm{x}_1) & 0 & \cdots & 0 & 0 \\ 0 & h(\mathrm{x}_2) & -h(\mathrm{x}_2) & \cdots & 0 & 0 \\ \vdots & \vdots & \vdots & & \vdots & \vdots \\ 0 & 0 & 0 & \cdots & -h(\mathrm{x}_{K-1}) & 0 \\ 0 & 0 & 0 & \cdots & h(\mathrm{x}_K) & -h(\mathrm{x}_K) \end{bmatrix}. \tag{6}$$

The quadratic norm form of (5) is

$$\min_{\alpha} \| X\alpha - Y \|^2, \ s.t. \ Z\alpha = 0. \tag{7}$$

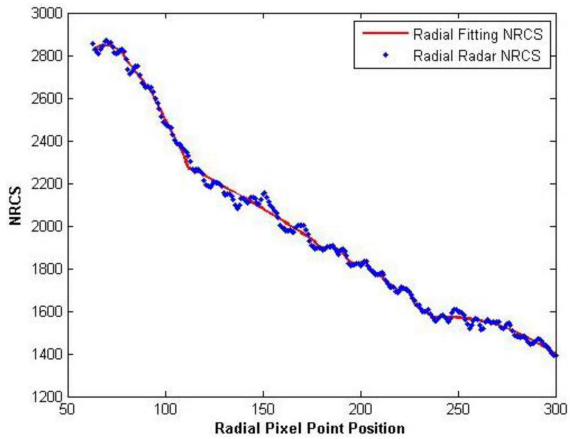

Fig. 10. Distributions of radar radial NRCS and fitting NRCS.

The Lagrange function is established for (7)

$$L(\alpha,\lambda) = \| X\alpha - Y \|^2 + 2\lambda^T Z\alpha \tag{8}$$

whereλ is the column vector constraint parameter, $\lambda = [\lambda_1, \lambda_2, \cdots, \lambda_K]^T$. From the extreme and necessary conditions of the multivariate function for (8), we obtain

$$\begin{cases} \frac{\partial L}{\partial \alpha} = 2X^T(X\alpha - Y) + 2Z^T\lambda = 0 \\ \frac{\partial L}{\partial \lambda} = Z\alpha = 0 \end{cases}. \tag{9}$$

From the first expression of (10), we have

$$\alpha = \hat{\alpha} - (\mathrm{X}^T\mathrm{X})^{-1} Z^T\lambda \tag{10}$$

where$\hat{\alpha} = (X^TX)^{-1}X^TY$. Substituting (10) into (8) yields

$$\lambda = \left[Z(X^TX)^{-1}Z^T \right]^{-1} Z\hat{\alpha}. \tag{11}$$

By substituting (11) into (10), we then obtain the solution for the least-squares regression coefficient α. According to the radar imaging mechanism, the dataset Ω_k could ensure that $(X_k^T X_k)^{-1}$in (10) is nonsingular, and Z is nonzero. Thus, α has a unique solution, and the fitting function $f(x)$ is finally obtained.

Step 4: Calculate the mean absolute errorS_k of each curve and the absolute error e_i of each point

$$S_k = \frac{1}{n_k} \sum_{i=1}^{n_k} \left| f_k(x_i^k) - y_i^k \right| \tag{12}$$

$$e_i = \left| f_k\left(x_i^k\right) - y_i^k \right| \tag{13}$$

where $k = 1, 2 \cdots K{+}1$, $i = 1, 2, \cdots n$. If $e_i{>}\mathrm{S}_k\&e_{i+1}{>}\mathrm{S}_k\&e_{i+2}{>}\mathrm{S}_k$, set up a subsection at point e_i again, and then implement step 5, otherwise go to step 6.

Step 5: Set up a subsection at point e_i for dataset Ω, and implement step 2.

Step 6: For a marine *X*-band radar image NRCS $\sigma(\theta_i, \mathrm{r}_j)$, the corrected radar image NRCS $\sigma'(\theta_i, \mathrm{r}_j)$is defined as

$$\sigma'\left(\theta_i, r_j\right) = \sigma\left(\theta_i, r_j\right) - f(x). \tag{14}$$

Fig. 10 shows the distributions of the radar radial NRCS y and fitting NRCS $f(x)$ in step 3, in which the two curves almost overlap. The correlation coefficient is 0.9986, with a bias of 0.83 and a standard deviation of 22.19, which demonstrates that $f(x)$ can approximately replace the radar radial normalized NRCS y.

The corrected radar image for step 6 is shown in Fig. 11(b). Since the correction reduces the effect of radial attenuation in the wave imaging, the wave streaks exhibit more uniform radial distributions than the original wave streaks in Fig. 11(a). The corrected marine radar image sequences are $g(\theta, r, t)$, in which $\theta$is the azimuth angle, $r$is the radial position, and t is the time-axis image sequence.

Based on a closest point interpolation approach, the Cartesian coordinate image sequence $g(x, y, t)$ can be transformed from $g(\theta, r, t)$ to$g(x, y, t)$, which is a 3-D space coordinate. By integrating a set of corrected marine radar image sequences according to 1, we obtain the static feature image of the sea surface $g(x, y)$.

The corrected static feature image is shown in Fig. 11(d). Compared to the uncorrected wind streak image in Fig. 11(c), the wind streaks have a more uniform distribution across the sea surface; hence, this method weakens the radial attenuation effect on wind direction retrieval.

C. ES Method for Wind Direction Retrieval

To obtain the wind streak ES from corrected radar image sequences, an ES scale separation filter that relates the wind streak scale must be established. The wind direction information is then retrieved based on the characteristics of the wind streak.

For a corrected radar image sequence, the ES of the sea surface static feature image is derived using the 2-D discrete fast Fourier transform (2-D FFT). The ES of the sea surface static feature image can be obtained using a vector absolute function

$$\begin{aligned} &A(k_x, k_y) \\ &= \sqrt{[\mathrm{Re}(F(k_x, k_y))]^2 + [\mathrm{Im}(F(k_x, k_y))]^2} \end{aligned} \tag{15}$$

where$A(k_x, k_y)$ contains signals at different wavelengths, and the relationship between wavelength and frequency wave number is

$$k = \frac{2\pi}{L} \tag{16}$$

where *k* is the ES wave number, $k = \sqrt{k_x^2 + k_y^2}$, $(k_x, k_y)$are the coordinates of the ES domain, and *L* is the streak wavelength.

The wind streak wavelength scale has a particular range. Through the theoretical research and data experimentation in Section III, the scale of the wind streak was determined to range from 200 to 500 m. Suppose L_d is the lower limit, i.e., $L_d = 200$ m, and L_t is the upper limit, i.e., $L_t = 500$ m. According to (16), the lower limit ES wave number $k_d$is

$$k_d = \frac{2\pi}{L_t} \tag{17}$$

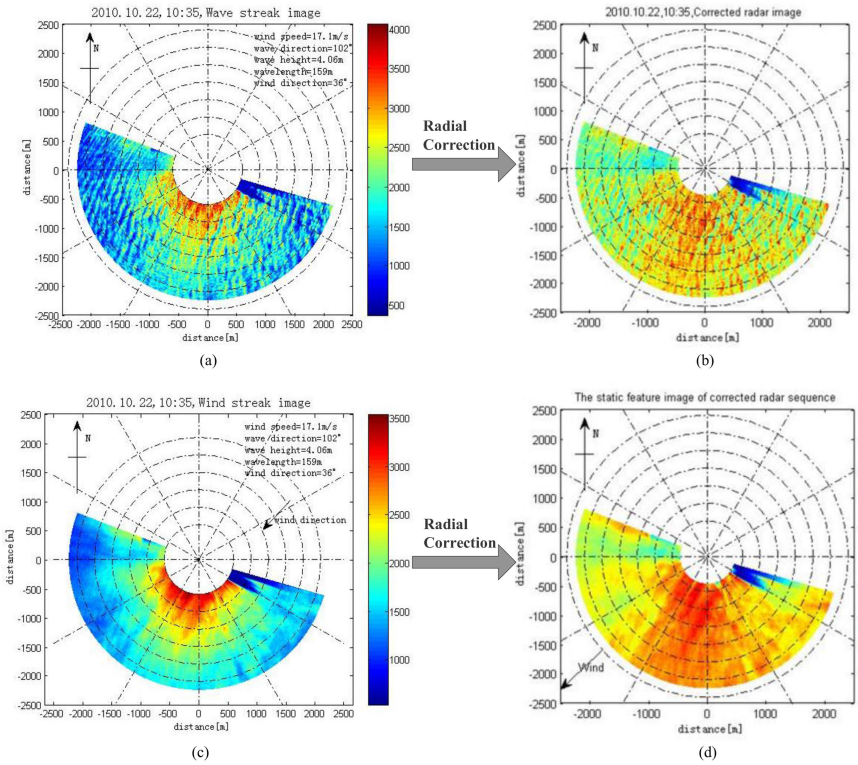

Fig. 11. Radial correction results of wave streak and wind streak images. (a) Wave streak image. (b) Corrected wave streak image. (c) Wind streak image. (d) Corrected wind streak image.

and the upper limit $k_t$is

$$k_t = \frac{2\pi}{L_d}. \tag{18}$$

To extract the ES of the wind streak, we designed an ES scale separation filter based on the lower and upper limits of the ES wave number as well as the characteristics of the sea surface static feature. The mathematical model is

$$I(k_x, k_y) = \begin{cases} A(k_x, k_y)(\sqrt{{k_x}^2 + {k_y}^2} \in [|k_d|, |k_t|]) \\ 0\,(\text{else}) \end{cases} \tag{19}$$

where $I(k_x, k_y)$ is the ES of the wind streaks. Fig. 12 shows the filter bandwidth shape, in which the inner boundary represents the lower limit $k_d = 0.0125rad/s$, the outer boundary represents the upper limit $k_t = 0.0628rad/s$, and the shaded area represents the reserved ES area.

Fig. 13 is the filtered wind streak ES for Fig. 11(b). The captured wind streak image is shown in Fig. 13(a), and the energy value distribution is shown in Fig. 13(b). Based on the symmetry and periodicity of the Fourier transform, we can determine that the ES $I(k_x, k_y)$ is symmetric in terms of the first and third quadrants, as well as the second and fourth quadrants. Note that Fig. 13(c) shows that the connecting line of the two concentrated energy areas is perpendicular to the wind streak. Thus, based on the theory that small-scale wind streaks in line with wind direction, the vertical direction of the connecting line is parallel to the wind streak direction, i.e., the wind direction W_d.

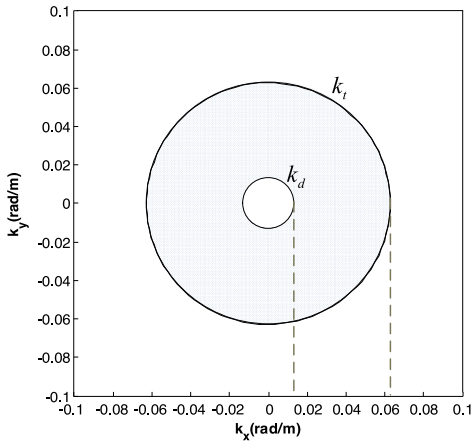

Fig. 12. Filter bandwidth illustration. The inner boundary represents the lower limit $k_d = 0.0125rad/s$, the outer ring represents the upper limit $k_t = 0.0628rad/s$, and the shaded area represents the reserved ES area.

Due to the ship heading effect, the true sea surface wind direction must be calibrated as shown as follows:

$$\mathrm{N_w} = |\theta_c| + |\alpha| + |W_d| \tag{20}$$

where N_w is the true retrieved wind direction relative to north, $\theta_c$is the central angle of a selected area, $W_d$is the retrieved wind direction with the 180° ambiguity removed, and $\alpha$is the ship heading direction.

The retrieved wind direction has the 180°ambiguity problem because the vertical direction of the connecting line has two

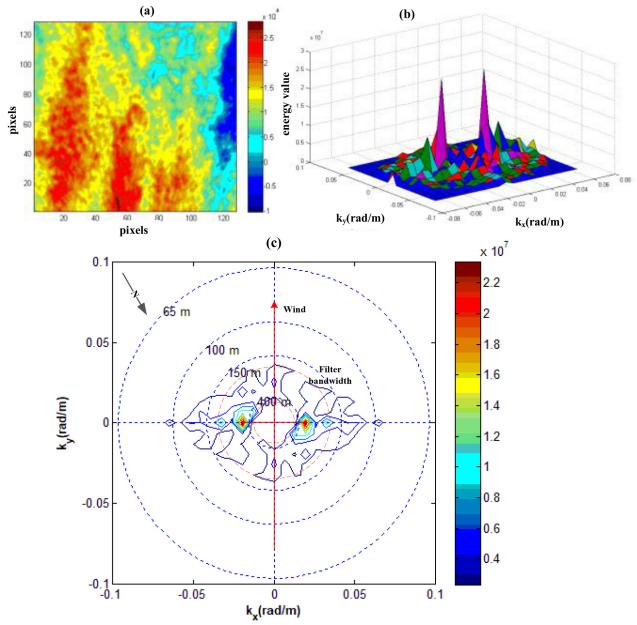

Fig. 13. Filtered wind streak ES. (a) Captured wind streak image. (b) Energy value distribution. (c) Wind direction perpendicular to the connecting line of the two concentrated energy areas.

different 180°directions. The 180° ambiguities can be removed in one of two means. The directional ambiguity can be removed using the dependence of the NRCS on the antenna look direction, because that for *X*-band radars operating at grazing incidence with HH polarization, a peak only exists in the upwind direction [2]. This method is only applicable if the ocean surface is imaged over the full azimuth, which is often not the case.

For another 180° ambiguity removal problem with wind direction, the wind wave directions obtained by 3-D FFT on image sequence inversion can be applied [16]. Generally, there is an angle of 10°–20° between the wind direction and the real sea wind direction. The 180° ambiguity can be removed by keeping the direction consistent with the wind information quadrant. This method solves the 180° ambiguity problem by using the marine radar image and has no strict limitation on the image coverage area, so it is convenient for straightforwardly using in marine environment monitoring platform.

V. Data Test

The experimental data were collected from the radar instrumentation and a vane anemometer. In Section IV, we tested the ES method using a single set of data collected on October 22, 2010. In this section, we will test several sets of data collected during October 2010 and December 2010. From a sum of 1634 measurements, 140 groups of data had to be excluded due to rain or the effects of Typhoon Megi passed. The remaining 1494 datasets had wind speeds ranging from just above 3 m/s to almost 17 m/s.

A. Wind Direction Retrieval

The point series in Fig. 14 shows the wind direction obtained from the ES method and measured by the anemometer vane. The

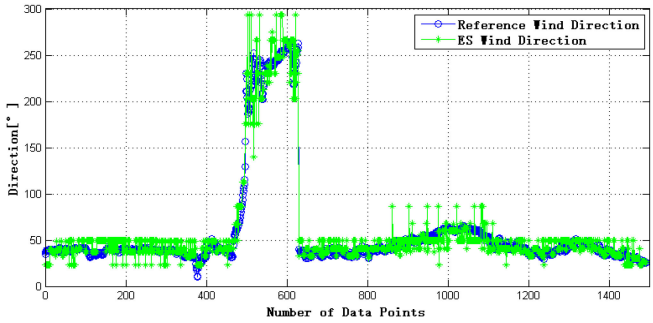

Fig. 14. Wind direction point series obtained from the ES method. (The blue curve with the open points represents the wind direction measured by the vane anemometer.)

radar retrieved direction and *in situ* vane wind direction exhibit similar trends in this figure. At the sampling points 1–500 and 630–1494, although the ES wind direction fluctuated slightly relative to the reference wind direction, its distribution was generally consistent with the reference wind direction. For sampling points 500–630, although the sea surface wind displayed a 180° reversal, backing from northeast to southwest due to the typhoon passed, the ES algorithm still performed well, exhibiting good stability.

Fig. 15 shows corresponding scatter plots of the radar results and anemometer measurements. In Fig. 15(a), for all 1634 sets of data, the correlation coefficient was found to be 0.89, with a bias of 4.02° and a standard deviation of 27.04°. For the with the 1494 sets of rain-free data, the correlation coefficient was found to be 0.98, with a bias of 1.68° and a standard deviation of 12.13°. The red points are the results from the rainfall data, which basically fluctuated between 0° and 200°, indicating that the ES-retrieved direction diverged dramatically from the reference wind direction. It demonstrates that the ES method is incapable of retrieving wind direction from rain-contaminated images. Fig. 15(b) shows the rain-contaminated and rainfall-free data error density distribution. After removing the rainfall images, the data error was more centralized and distributed about zero, and the fitting curve was steeper. Contrary to this, the $\sigma$of the error result influenced by rainfall was larger, and the error distribution was more dispersed. The OZPP rainfall identification algorithm can effectively eliminate the influence of rainfall data (shown in red color points). When the surface wind direction was approximately 50°, there was a larger overlap region, the ES shows acceptable performance (the points uniformly distribute around the fitting curve). When the wind direction was over 200°; some individual sample points of the ES wind direction deviated from the reference direction. A check of the original image data revealed that these were caused by the incomplete removal of rainfall-influenced images.

B. Sensitivity Analysis

Fig. 16 shows the small-scale wind streaks on the radar image with wind speed of 3, 6, 10, 12.6, 15, 17.5, 19, and 20.1 m/s. When the wind speed exceeds 6 m/s, it shows obvious wind scale streaks characteristics. Fig. 17 shows the radar and *in situ* wind direction errors at different wind speeds. The left hand of

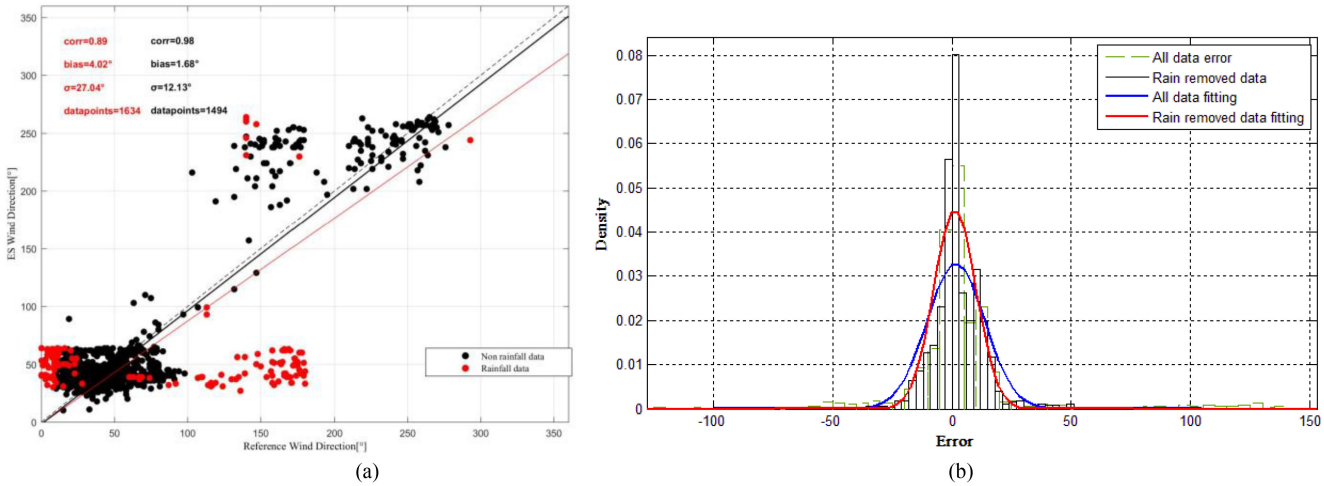

Fig. 15. Scatter plot of *in situ* wind direction versus radar wind direction. (a) Rain-contaminated and rain-free data results. (b) Rain-contaminated and rain-free data error density distribution fitting.

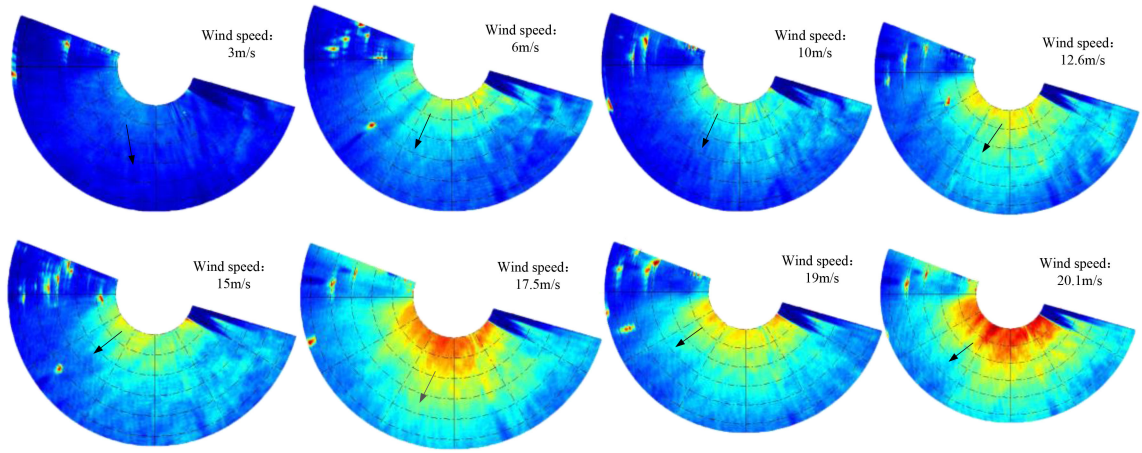

Fig. 16. Small-scale wind streaks on the radar image at different wind speed. (Wind speeds are 3, 6, 10, 12.6, 15, 17.5, 19, and 20.1 m/s, respectively. The black arrow indicates the wind direction of the sea surface at this time.)

the vertical axis in each subplot is the wind speed, in increments of 0–5, 5–10, 10–15, and 15–20 m/s, while the right-hand side is wind direction error, in increments of −110°–110°,−70°–70°,−65°–45°, and −25°–25°. This figure shows that most of the wind direction data fell within the range of 10–15 m/s, and the error decreased with wind speed increasing, which is in accordance with the theory in [17] that small-scale wind streaks increase as the wind speed increases. The increase of the small-scale streak size can effectively improve the inversion accuracy of the ES.

The wind direction error between the radar and vane anemometer is shown in Fig. 18, in which the shaded area represents measurement speed data by vane. For the 1494 groups of data, the absolute value of the error was smaller than 20°. The inversion error of the ES sea surface wind direction at sampling points 500–630 was large, as shown within the red rectangle. In the period, the reference wind speed dramatically changed from 15 to 5 m/s. Owing to the change of wind speed, there were numerous sea-level surges, which collapsed the small-scale wind streak characteristics, thereby diminishing the accuracy of the inversion algorithm. The error of the ES holds stable when the sea surface wind speed was between 10 and 15 m/s. Although the wind streak scale increases with increasing wind speed, it exerts little influence on the ES method. This is because a variety of scale characteristics have been considered in the design of band-pass filter for ES method, so together eliminate the influence caused by the change of sea surface wind speed. In addition, it is no longer necessary to conduct data processing in spatial domain, which is a more effective and robust approach for counteracting the influence of sea surface conditions.

Fig. 19 shows the bias (black curve) and standard deviation (blue curve) of wind direction between radar and vane anemometer, plotted against wind speed. The dependence of the bias on wind speed was negligible, although the standard deviation grew larger with increasing wind speed for speeds smaller than10 m/s, and then decreased for speeds larger than10 m/s. If the wind speed is over10 m/s, it will be easy to retrieve wind direction from radar data because the wind streaks are obvious. Under weak wind conditions, the NRCS is less indicative of atmospheric processes than oceanic processes, such as bathymetric effects

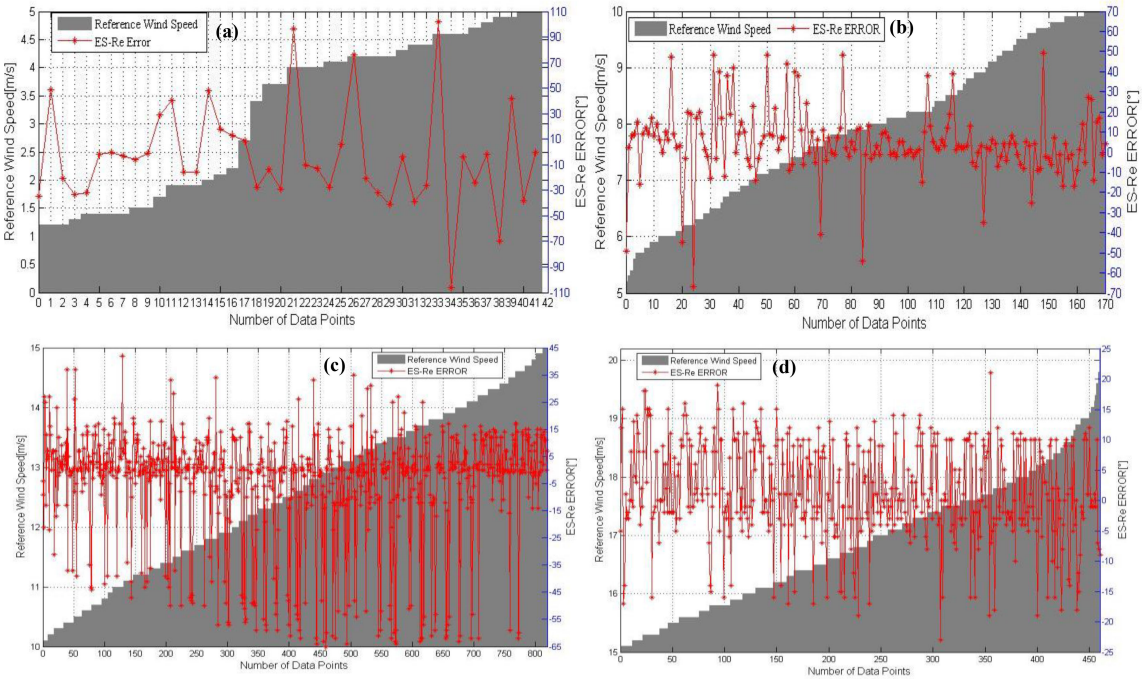

Fig. 17. Wind direction error between radar wind direction and *in situ* wind direction at different wind speeds. (a) 0–5 m/s. (b) 5–10 m/s. (c) 10–15 m/s. (d) 15–20 m/s.

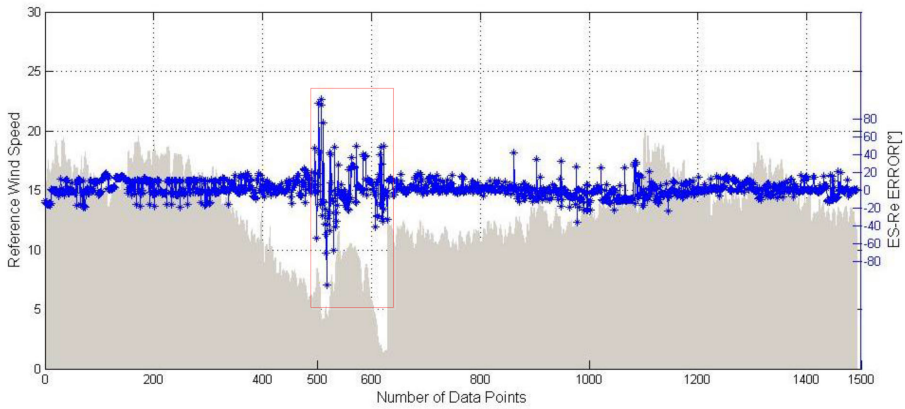

Fig. 18. Wind direction error between radar wind direction and *in situ* wind direction.

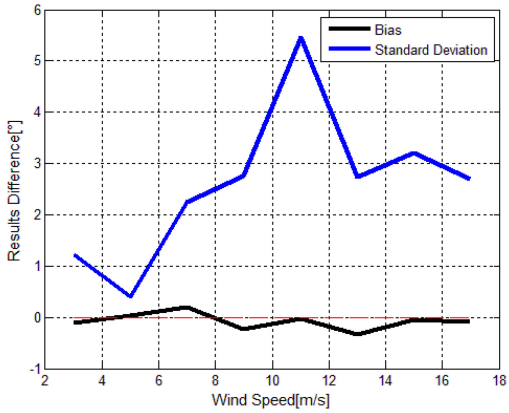

Fig. 19. Bias (black line) and standard deviation (blue line) of radar and *in situ* wind direction difference, plotted against wind speed.

and current shear. In such cases, the wind directionality of the NRCS is dominated by wind-driven ripple waves, a single peak will appear in the upwind direction for HH polarization and grazing incidence. Under strong wind conditions, the NRCS is majorly affected by gusts caused by wind speed changes.

Table I compares the method proposed in this study with three classic methods. All methods use HEU wave monitoring system data to retrieve sea surface wind. It shows that the ES is superior in terms with inversion precision. At the same time, the ES is less affected by wind speed. The more prominent advantage is that this method can obtain the energy information and ES of the sea surface wind field, providing special information for the subsequent inversion of sea surface wind speed and marine meteorological information.

Gusts generate varying amounts of wind shear on thousands of meters of the air–sea boundary layer, and nonuniform wind

TABLE I
COMPARISON OF THE PROPOSED ES METHOD WITH CLASSIC WIND MEASUREMENT TECHNIQUES

Method	Wind spectrum estimation	Wind speed influence	Correlation coefficient	RMS difference (°)	Deviation (°)	Running time (s)	Images required
Energy spectrum	√	Low	0.98	12.13	1.68	18.4	Multiple
Single curve fitting	×	High	0.95	18.45	3.58	6.5	Single
Local gradient	×	High	0.98	17.33	1.18	27.1	Single
Optical flow	×	Low	0.51	54	12.75	38.3	Multiple

shear acting on irregular atmospheric turbulence will lead to banded turbulence. This banded turbulence causes sea surface roughness, leading to NRCS in the form of wind streaks that exist in marine radar image sequences. In this study, we could not test the inversion results at wind speeds exceeding 18 m/s due to the limitations of the collected data.

VI. CONCLUSION

In this study, a new ES method for retrieving wind direction from marine *X*-band radar image sequences was proposed. This method provides an improved OZPP rainfall recognition algorithm that can more accurately identify and remove rainfall pollution images, and then weaken the attenuation of radial NRCS to allow clearer wind streak images. Moreover, since this method was designed based on the wind streak ES, it requires no extra image processing in spatial domain.

Compared to the *in situ* radar radial NRCS, the proposed method obtains a fitting NRCS with a bias of 0.83 and a standard deviation of 22.19, while the correlation coefficient between the two NRCS is as high as 0.9986. For wind direction, compared to the data measured by the *in situ* vane anemometer, this method has a correlation coefficient of 0.98, with a bias of 1.68° and a standard deviation of 12.13°. After using the OZPP algorithm, the root-mean-square error of the wind directions retrieved reduces by 55%. The new method can fit different ocean states since it is unnecessary to know the wind streak spacing in advance. The results show that if the wind speed is over 10 m/s, the wind streaks will be more obvious, and the proposed method exerts superior performance correspondingly.

In the future, we will improve the OZPP algorithm to make the rain-contaminated images fit the ES method after removing the effect of rainfall. Also, a more proper height conversion coefficient of wind speed between the sea surface and measurement position needs to be determined. The feasibility of the ES method under typhoon condition will be the focus of our further research.

REFERENCES

[1] C. Zhao, Z. Chen, J. Li, L. Zhang, W. Huang, and E. W. Gill, "Wind direction estimation using small-aperture HF radar based on a circular array," *IEEE Trans. Geosci. Remote Sens.*, vol. 58, no. 4, pp. 2745–2754, Apr. 2020.

[2] R. Vicen-Bueno, J. Horstmann, E. Terril, T. de Paolo, and J. Dannenberg, "Real-time ocean wind vector retrieval from marine radar image sequences acquired at grazing angle," *J. Atmos. Ocean. Technol.*, vol. 30, no. 1, pp. 127–139, 2013.

[3] S. Lehner, J. Schulz-Stellenfleth, B. Schättler, H. Breit, and J. Horstmann, "Wind and wave measurements using complex ERS-2 SAR wave mode data," *IEEE Trans. Geosci. Remote Sens.*, vol. 38, no. 5, pp. 2246–2257, Sep. 2000.

[4] H. Fang, W. Perrie, G. Fan, T. Xie, and J. Yang, "Ocean surface wind speed retrieval from C-band quad-polarized SAR measurements at optimal spatial resolution," *Remote Sens. Lett.*, vol. 12, no. 2, pp. 155–164, 2021.

[5] L. R. Wyatt *et al.*, "Operational wave, current, and wind measurements with the pisces HF radar," *IEEE J. Ocean. Eng.*, vol. 31, no. 4, pp. 819–834, Oct. 2006.

[6] H. Fang, T. Xie, W. Perrie, L. Zhao, J. Yang, and Y. He, "Ocean wind and current retrievals based on satellite SAR measurements in conjunction with buoy and HF radar data," *Remote Sens.,* vol. 9, no. 12, 2017, Art. no. 1321.

[7] J. Horstmann, J. C. N. Borge, J. Seemann, R. Carrasco, and B. Lund, "Wind, wave, and current retrieval utilizing X-band marine radars," in *Coastal Ocean Observing Systems.* Academic: Orlando, FL, USA, 2015, pp. 281–304.

[8] B. Lund, H. C. Graber, and R. Romeiser, "Wind retrieval from shipborne marine X-band radar data," *IEEE Trans. Geosci. Remote Sens.*, vol. 50, no. 10 I, pp. 3800–3811, Oct. 2012.

[9] Y. Wei, Z. Lu, G. Yuan, Z. Fang, and Y. Huang, "Sparsity adaptive matching pursuit detection algorithm based on compressed sensing for radar signals," *Sensors (Switzerland)*, vol. 17, no. 5, 2017, Art. no. 1120.

[10] P. Liu, Y. Li, B. Liu, P. Chen, and J. Xu, "Semi-automatic oil spill detection on X-band marine radar images using texture analysis, machine learning, and adaptive thresholding," *Remote Sens.,* vol. 11, no. 7, 2019, Art. no. 756.

[11] A. A. Al-Habashneh, C. Moloney, E. W. Gill, and W. Huang, "The effect of radar ocean surface sampling on wave spectrum estimation using X-band marine radar," *IEEE Access*, vol. 6, pp. 17570–17585, Mar. 2018.

[12] C. M. Senet, J. Seemann, S. Flampouris, and F. Ziemer, "Determination of bathymetric and current maps by the method DiSC based on the analysis of nautical X-band radar image sequences of the sea surface (November 2007)," *IEEE Trans. Geosci. Remote Sens.*, vol. 46, no. 8, pp. 2267–2279, Aug. 2008.

[13] C. Shen, W. Huang, E. W. Gill, R. Carrasco, and J. Horstmann, "An algorithm for surface current retrieval from X-band marine radar images," *Remote Sens.,* vol. 7, no. 6, pp. 7753–7767, 2015.

[14] Z. Chen, Y. He, and B. Zhang, "An automatic algorithm to retrieve wave height from X-band marine radar image sequence," *IEEE Trans. Geosci. Remote Sens.*, vol. 55, no. 9, pp. 5084–5092, Sep. 2017.

[15] J. C. Nieto-Borge, K. Hessner, P. Jarabo-Amores, and D. De La Mata-Moya, "Signal-to-noise ratio analysis to estimate ocean wave heights from X-band marine radar image time series," *IET Radar, Sonar Navigation,* vol. 2, no. 1, pp. 35–41, 2008.

[16] X. Liu, W. Huang, and E. W. Gill, "Wave height estimation from shipborne X-band nautical radar images," *J. Sensors*, vol. 2016, Jul. 2016, Art. no. 1078053.

[17] Y. Liu, W. Huang, E. W. Gill, D. K. Peters, and R. Vicen-Bueno, "Comparison of algorithms for wind parameters extraction from shipborne x-band marine radar images," *IEEE J. Sel. Topics Appl. Earth Obs. Remote Sens.*, vol. 8, no. 2, pp. 896–906, Feb. 2015.

[18] W. Huang *et al.*, "Ocean wind and wave measurements using X-band marine radar: A comprehensive review," *Remote Sens.,* vol. 9, no. 12, Jan. 2017, Art. no. 1261.

[19] H. Hatten, J. Seemann, J. Horstmann, and F. Ziemer, "Azimuthal dependence of the radar cross section and the spectral background noise of a nautical radar at grazing incidence," *Int. Geosci. Remote Sens. Symp.*, vol. 5, pp. 2490–2492, 1998.

[20] H. Dankert, J. Horstmann, A. K. Magnusson, and W. Rosenthal, "Ocean winds retrieved from X-band radar-image sequences," *Int. Geosci. Remote Sens. Symp.*, vol. 2, pp. 1261–1263, 2003.

[21] X. Liu, W. Huang, and E. W. Gill, "Wind direction estimation from rain-contaminated marine radar data using the ensemble empirical mode decomposition method," *IEEE Trans. Geosci. Remote Sens.*, vol. 55, no. 3, pp. 1833–1841, Mar. 2017.

[22] H. Dankert, J. Horstmann, and W. Rosenthal, "Ocean surface winds retrieved from marine radar-image sequences," *Int. Geosci. Remote Sens. Symp.*, vol. 3, pp. 1903–1906, 2004.
[23] H. Dankert, J. Horstmann, and W. Rosenthal, "Ocean wind fields retrieved from radar-image sequences," *J. Geophys. Res. Ocean.*, vol. 108, no. 11, pp. 2150–2152, 2003.
[24] H. Dankert and J. Horstmann, "A marine radar wind sensor," *J. Atmos. Ocean. Technol.*, vol. 24, no. 9, pp. 1629–1642, 2007.
[25] W. Huang, Y. Liu, and E. W. Gill, "Texture-analysis-incorporated wind parameters extraction from rain-contaminated X-band nautical radar images," *Remote Sens.,* vol. 9, no. 2, 2017, Art. no. 166.
[26] X. Liu, W. Huang, and E. W. Gill, "Estimation of significant wave height from X-band marine radar images based on ensemble empirical mode decomposition," *IEEE Geosci. Remote Sens. Lett.*, vol. 14, no. 10, pp. 1740–1744, Oct. 2017.
[27] G. Zhang, X. Li, W. Perrie, B. Zhang, and L. Wang, "Rain effects on the hurricane observations over the ocean by C-band synthetic aperture radar," *J. Geophys. Res. Oceans*, vol. 121, no. 1, pp. 14–26, 2016.
[28] F. Xu, X. Li, P. Wang, J. Yang, W. G. Pichel, and Y. Q. Jin, "A backscattering model of rainfall over rough sea surface for synthetic aperture radar," *IEEE Trans. Geosci. Remote Sens.*, vol. 53, no. 6, pp. 3042–3054, Jun. 2015.
[29] X. Chen, W. Huang, C. Zhao, and Y. Tian, "Rain detection from X-band marine radar images: A support vector machine-based approach," *IEEE Trans. Geosci. Remote Sens.*, vol. 58, no. 3, pp. 2115–2123, Dec. 2020.
[30] X. Chen and W. Huang, "Identification of rain and low-backscatter regions in X-band marine radar images: An unsupervised approach," *IEEE Trans. Geosci. Remote Sens.*, vol. 58, no. 6, pp. 4225–4236, Jun. 2020.
[31] X. Chen, W. Huang, M. C. Haller, and R. Pittman, "Rain-contaminated region segmentation of X-band marine radar images with an ensemble of segNets," *IEEE J. Sel. Topics Appl. Earth Observ. Remote Sens.*, vol. 14, pp. 141–154, Dec. 2020.
[32] Z. Chen, Y. He, B. Zhang, and Y. Ma, "A method to correct the influence of rain on X-band marine radar image," *IEEE Access*, vol. 5, pp. 25576–25583, Nov. 2017.
[33] Y. Zhao, X. M. Li, and J. Sha, "Sea surface wind streaks in spaceborne synthetic aperture radar imagery," *J. Geophys. Res. Oceans*, vol. 121, no. 9, pp. 6731–6741, 2016.
[34] K. Wang *et al.*, "Numerical simulation of Bohai oil spill in the winter sea ice period," *China Ocean Eng.,* vol. 33, no. 2, pp. 185–197, 2019.
[35] S. Zecchetto, "Wind direction extraction from SAR in coastal areas," *Remote Sens.,* vol. 10, no. 2, 2018, Art. no. 261.
[36] J. Horstmann, S. Lehner, W. Koch, and R. Tonboe, "Computation of wind vectors over the ocean using spaceborne synthetic aperture radar," *Johns Hopkins APL Tech. Dig.*, vol. 21, no. 1, pp. 100–107, 2000.
[37] C. Wang *et al.*, "Classification of the global Sentinel-1 SAR vignettes for ocean surface process studies," *Remote Sens. Environ.*, vol. 234, 2019, Art. no. 111457.
[38] Y. Wang and W. Huang, "An algorithm for wind direction retrieval from X-band marine radar images," *IEEE Geosci. Remote Sens. Lett.*, vol. 13, no. 2, pp. 252–256, Mar. 2016.
[39] W. Alpers and B. Brummer, "Atmospheric boundary layer rolls observed by the synthetic aperture radar aboard the ERS-1 satellite," *J. Geophys. Res.*, vol. 99, no. C6, pp. 613–621, 1994.
[40] X. Li *et al.*, "Coexistence of atmospheric gravity waves and boundary layer rolls observed by SAR," *J. Atmos. Sci.,* vol. 70, no. 11, pp. 3448–3459, 2013.
[41] W. Koch, "Directional analysis of SAR images aiming at wind direction," *IEEE Trans. Geosci. Remote Sens.*, vol. 42, no. 4, pp. 702–710, Apr. 2004.

Hui Wang received the B.Sc. from the Tianjin University of Technology and Education, Tianjin, China, in 2008, and the Ph.D. degree in navigation guidance from Harbin Engineering University, Harbin, China, in 2016.

Currently, she is with Electronics and Information School, Jiangsu University of Science and Technology, Zhenjiang, China. His main research interests include marine radar image processing, marine integrated hydrological remote sensing, and information forecasting technology.

Haiyang Qiu received the B.Sc. and Ph.D. degrees in navigation guidance from Harbin Engineering University, Harbin, China, in 2010 and 2016, respectively.

He is currently a Faculty with the School of Electronics and Information School, Jiangsu University of Science and Technology, Zhenjiang, China. From 2013 to 2014, he was a Visiting Scholar with the Queensland University of Technology, Brisbane, QLD, Australia. His major research interests include marine vehicles navigation, image processing and inertial aided underwater SLAM, distributed mapping with multiple agents.

Zhizhong Lu received the B.Sc. degree from Fudan University, Shanghai, China, the M.Sc. and Ph.D. degrees in navigation guidance from Harbin Engineering University, Harbin, China, in 1989, 2001, and 2008, respectively.

Currently, he is a Professor with the College of Automation, Harbin Engineering University. His main research interests include marine integrated hydrological remote sensing and information forecasting technology.

Lei Wang received the Ph.D. degree in electronic engineering and computer science from Queensland University of Technology (QUT), Brisbane, QLD, Australia, in 2015.

He is currently an Associate Research Fellow with the State Key Laboratory of Information Engineering in Surveying, Mapping and Remote Sensing (LIESMARS), Wuhan University, Wuhan, China. His research interests include LEO navigation augmentation system, GNSS precise positioning, and LEO orbit determination.

Rizwan Akhtar received the Ph.D. degree in communication and information engineering from the University of Electronic Science and Technology of China, Chengdu, China, in 2014.

He is working as an Associate Professor with the School of Electronics and Information, Jiangsu University of Science and Technology, Zhenjiang, China. He has published more than 30 research articles in international journals and conferences. His research interests include IP2P networks, intelligent transportation systems, IoT, IOV, under water wireless sensor networks, ship communication, and navigation systems.

Yanbo Wei received the B.Sc. degree from the Anyang Institute of Technology, Anyang, China, in 2011, and the Ph.D. degree in navigation guidance from Harbin Engineering University, Harbin, China, in 2017.

From 2014 to 2016, he was a Visiting Student with the Department of Electronic and Computer Engineering, McMaster University, Hamilton, ON, Canada. He is currently a Lecturer with the College of Physical and Electronic Information, Luoyang Normal University, Luoyang, China. His main research interest includes retrieving wave information from *X*-band marine radar images.